Mon. Not. R. Astron. Soc. **000**, 000–000 (0000) Printed 2 February 2022 (MN LATEX style file v2.2)

The properties of powerful radio sources at 90 GHz

M.J. Hardcastle[1,2] and L.W. Looney[3]
[1] *School of Physics, Astronomy and Mathematics, University of Hertfordshire, College Lane, Hatfield, Hertfordshire AL10 9AB*
[2] *Department of Physics, University of Bristol, Tyndall Avenue, Bristol BS8 1TL*
[3] *Department of Astronomy, University of Illinois, 1002 West Green Street, Urbana, IL 61801, U.S.A.*

arXiv:0804.3369v1 [astro-ph] 21 Apr 2008

2 February 2022

ABSTRACT
We have observed a small sample of powerful double radio sources (radio galaxies and quasars) at frequencies around 90 GHz with the BIMA millimetre array, with the intention of constraining the resolved high-frequency spectra of radio galaxies. When combined with other sources we have previously observed and with data from the BIMA archive, these observations allow us for the first time to make general statements about the high-frequency behaviour of compact components of radio galaxies – cores, jets and hotspots. We find that cores in our sample remain flat-spectrum up to 90 GHz; jets in some of our targets are detected at 90 GHz for the first time in our new observations; and hotspots are found to be almost universal, but show a wide range of spectral properties. Emission from the extended lobes of radio galaxies is detected in a few cases and shows rough consistency with the expectations from standard spectral ageing models, though our ability to probe this in detail is limited by the sensitivity of BIMA. We briefly discuss the prospects for radio-galaxy astrophysics with ALMA.

Key words: radio continuum: galaxies – galaxies: jets

1 INTRODUCTION

Although they are the dominant radio source population in the sky at low radio frequencies, steep-spectrum extragalactic radio sources (radio galaxies and lobe-dominated radio-loud quasars) have been relatively poorly studied at millimetre wavelengths (corresponding to frequencies $\gtrsim 100$ GHz), although a good deal of work has been done on integrated flux density measurements of their flat-spectrum, jet-dominated counterparts (e.g. Edelson 1987). Where information on steep-spectrum radio sources at mm wavelengths is available in the literature (e.g. Steppe et al. 1988, 1995) it tends to be restricted to tables of integrated flux densities. This is presumably partly due to the intrinsic difficulty of mm-wave observations compared to those at 1–10 GHz, partly because the steep spectrum of most components of radio galaxies makes them harder to detect at higher frequencies, and partly because of a perception that there is little additional information to be gained at high frequencies.

High-frequency imaging observations of radio galaxies and quasars can have some astrophysical importance, however. In early work on the spectrum of the large-scale radio emission from powerful radio galaxies (FRIIs, Fanaroff & Riley 1974), it was found that their spectra, measured at centimetre wavelengths, systematically steepen with distance from the hotspots, inferred to be the sites of particle acceleration at each end of the source (e.g. Myers & Spangler 1985, Alexander & Leahy 1987). The steepening was interpreted as evidence for 'synchrotron ageing', whereby the synchrotron energy loss process depletes high-energy electrons in the source (e.g. Pacholczyk 1970, Jaffe & Perola 1973, Leahy 1991). If observations of spectral steepening in FRIIs are really a result of synchrotron ageing, then in principle resolved images of the radio spectra allow us to measure plasma age as a function of position in the source, which in turn allows the determination of quantities like total source age and expansion speed. However, the interpretation of the spectral steepening in FRIIs in terms of synchrotron ageing has been questioned more recently. Most dramatically, Katz-Stone, Rudnick & Anderson (1993) showed that the detailed centimetre-wave spectrum of the extended 'lobe' emission in the powerful FRII source Cygnus A (3C 405) is not consistent with any conventional ageing model, arguing instead that the observations are consistent with a single, curved electron energy spectrum seen in a varying magnetic field; this would imply that ageing is in fact a negligible effect in the lobes. Introducing inhomogeneities into the field strength or electron population also seems likely to undermine 'traditional' spectral ageing. Rudnick (1999) gives a summary of the theoretical and observational problems faced by ageing models.

One important constraint on all models would be observations at wavelengths shorter than the centimetre wavelengths typically used in observations of radio galaxies. The effects of ageing become greater as we go to shorter wavelengths; in particular, there should be a very strong difference between the short-wavelength spectra of regions near and far from the hotspots in the standard picture. However, only a few powerful radio galaxies have been imaged at these short wavelengths. Cygnus A, the brightest such object in the sky, has been observed with the Berkeley Illinois Maryland Association millimetre-wave interferometer (BIMA) on sev-

eral occasions (Wright & Birkinshaw 1984, Wright & Sault 1993) and with the IRAM 30-m telescope at 230 GHz (Salter et al. 1989). Wright & Sault (1993) commented briefly on the global spectrum of the lobes of Cygnus A at $\sim$ 90 GHz, but their result does not tell us anything about the *variation* of the centimetre-to-millimetre spectrum of the source as a function of position. More recently, we used BIMA to observe the radio galaxies 3C 123 and 3C 20 (Looney & Hardcastle 2000, Hardcastle & Looney 2001) at similar frequencies. We noted that the integrated spectrum of a part of the northern lobe of 3C 123 was inconsistent with an ageing model, leading us to suggest that particle acceleration might be ongoing in that region. An upper limit on the flux density of the southern lobe was consistent with ageing models, however. In 3C 20, the centimetre-to-millimetre spectrum of a part of the eastern lobe was very consistent with spectral ageing models, in contrast to the results of Katz-Stone et al.

In this paper we combine the results of this and other earlier work with new observations of a small sample of FRII radio sources using BIMA, taken in configurations intended to allow us to separate lobes from core, jet and hotspot emission. When combined with observations with the NRAO Very Large Array (VLA) and the Multi-Element Radio Linked Interferometer Network (MERLIN) the resulting database of objects allows us to make some general statements about the high-frequency spectral properties of components of FRIIs and about the viability of standard spectral ageing models. We also comment on the prospects for observations of radio galaxies with the Atacama Large Millimeter Array (ALMA).

J2000.0 co-ordinates are used throughout, and spectral index α is defined in the sense $S \propto \nu^{-\alpha}$. Resolutions quoted are the major $\times$ minor FWHM of elliptical restoring Gaussians (the Gaussian is circular if only one number is quoted) and the position angles quoted are the angle between the major axis and north, defined in the sense that positive angles indicate a rotation eastwards.

2 THE OBSERVATIONS

Our aim in making new observations was to detect the lobe-related emission seen in our observations of 3C 123 and 3C 20. Accordingly, we selected for observation FRII radio sources with high surface brightness, so as to maximize the prospects of detecting the comparatively low-surface-brightness lobes with BIMA. We chose our targets from the 3CRR sample (Laing, Riley & Longair 1983). After excluding compact-steep-spectrum sources, which BIMA cannot image usefully given their small angular size, and core-dominated objects, we obtained the sample listed in Table 1. The two sources we had previously observed, 3C 20 and 3C 123, would also have been selected from 3CRR by these criteria. 3C 405, our final object, is excluded from 3CRR because of its low Galactic latitude, but is of course of very high surface brightness at low frequency. Data for 3C 405, the B- and C-array components of the mosaiced observations discussed by Wright, Chernin & Forster (1997), were kindly supplied by Mel Wright.

The five new sources were then observed with BIMA[1]. Observational details are given for all eight of the FRIIs discussed in this paper in Table 2. Our strategy in each case was to observe with the BIMA configurations required to sample fully the largest-scale structure seen in the source at lower frequencies. We observed the largest sources with the BIMA D-array; the smallest source, 3C 295, only required B-array for full sampling, but we also used A-array to resolve the source. In all cases, the correlator was configured to give two 800-MHz bands around 86 GHz; for 3C 295, these were centred on 83.15 and 86.60 GHz, while for the other newly observed sources they were at 86.00 and 89.44 GHz.

The new data were calibrated in MIRIAD (Sault, Teuben & Wright 1995). Amplitudes were mostly calibrated by using observations of Mars and Uranus to bootstrap a nearby bright point source, which was then used as a phase calibrator. For the observations of 3C 295, we used 3C 273 as a flux calibrator, basing its flux density on monitoring observations, which gave a flux density at our observing frequency of 11 Jy; at A configuration we made frequent observations of a nearby bright quasar, J1419+543, to track short-timescale atmospheric phase variations. The similar strategy adopted for 3C 123 is discussed in detail in Looney & Hardcastle (2000). The error in the flux density calibration is likely to be of the order of 10 per cent.

The datasets at the various different BIMA configurations were then combined, and final images were made in AIPS using the IMAGR task, except for the observations of Cygnus A, where the joint deconvolution algorithms provided by MIRIAD were used to image each sideband, and the final images were combined in AIPS. For a typical source, where the longest baselines were provided by the B configuration, the full resolution of the combined datasets was about 3 arcsec, and the off-source noise at that resolution was between 0.5 and 1 mJy beam^{-1}. In Figs 1 to 8 we show images of all these sources.

Hardcastle et al. (2002) discuss B-array BIMA observations of three further FRII sources, one radio galaxy (3C 330) and two quasars (3C 263 and 3C 351). These objects were not selected for high lobe surface brightness, but for hotspot brightness: moreover, the B-array observations are not optimized for lobe detections, and so can only tell us about compact source components. We make use of these observations to increase our sample of core and hotspot measurements. Details of this additional sample are given in Table 3 and the observing parameters are given in Table 4. The two observing bands used were at 83.2 and 86.6 GHz. Images of these three sources are shown in Figs 9 to 11.

Table 1. The surface-brightness-selected sample of FRII radio sources

Source	Newly observed?	z	LAS (arcsec)	178-MHz flux density (Jy)
3C 20	N	0.174	53.6	46.8
3C 123	N	0.218	38	206.0
3C 220.1	Y	0.61	35	17.22
3C 295	Y	0.461	6	91.0
3C 388	Y	0.091	50	26.81
3C 401	Y	0.201	23.6	22.78
3C 405	N	0.0565	130	9660
3C 438	Y	0.290	22.6	48.72

Redshifts and 178-MHz flux densities for these sources come from Laing et al. (1983), updated to the more recent values given at http://3crr.extragalactic.info/ where appropriate, with the flux densities being given on the Baars et al. (1977) scale, except for 3C 405, where the flux density is the Baars et al. value.

[1] The BIMA array was operated by the Berkeley Illinois Maryland Association under funding from the U.S. National Science Foundation.

Table 2. Details of the BIMA observations of the surface-brightness-selected sample

Source	Array	Date	Duration (hours)	Frequency (GHz)
3C 20	B	1999 Oct 30	7.7	84.9
	C	1999 Oct 11	6.4	
3C 123	C	1996 Nov 02	9.9	107.8
	C	1996 Nov 06	8.8	
	B	1997 Feb 15	11.2	
	A	1996 Nov 27	10.1	
3C 220.1	B	2001 Feb 01	7.6	87.7
	C	2000 Nov 04	3.7	
	C	2000 Dec 06	4.2	
	D	2000 Oct 12	5.5	
3C 295	A	2000 Jan 26	10.6	84.9
	A	2000 Jan 31	8.6	
	A	2000 Feb 01	4.7	
	A	2000 Feb 02	10.3	
	A	2000 Feb 05	9.1	
	B	2000 Feb 23	5.7	
3C 388	B	2001 Jan 21	8.6	87.7
	C	2000 Nov 05	8.0	
	D	2000 Oct 05	6.0	
	D	2000 Oct 17	3.2	
3C 401	B	2001 Feb 14	8.1	87.7
	C	2000 Nov 20	8.0	
3C 405	B	1997 Apr 26	8.6	87.7
	C	1996 Mar 31	6	
3C 438	B	2001 Feb 27	6.0	87.7
	C	2000 Oct 26	7.4	
	C	2000 Nov 28	6.3	

Only observations that were used in the analysis are listed. Durations are for the entire run, including calibration observations; this indicates the coverage of the uv plane obtained. Typical on-source integration times are 60 per cent of the run time for C and D configurations, 50 per cent for B configuration, and 30 per cent for A configuration. The frequency listed is the effective frequency of the final images, the mean of the central frequencies of the two BIMA bands used in each case.

Table 3. The additional sample of FRII radio sources

Source	Newly observed?	z	LAS (arcsec)	178-MHz flux density (Jy)
3C 263	N	0.6563	51	16.6
3C 330	N	0.5490	60	30.3
3C 351	N	0.371	74	14.9

Notes as for Table 1.

Table 4. Details of the BIMA observations of the additional sample

Source	Array	Date	Duration (hours)	Frequency (GHz)
3C263	B	2002 Feb 03	8.0	84.9
3C330	B	2002 Feb 08	4.8	84.9
3C351	B	2002 Feb 10	7.5	84.9

Notes as for Table 2.

3 RESULTS: COMPONENTS OF RADIO SOURCES

As Figs 1–11 show, BIMA detects emission from the cores, jets, hotspots and (in some cases) the lobes of the sources in the samples. In this section we discuss the trends seen for each of these components. Throughout we refer to the BIMA observing frequency for simplicity as 90 GHz, though the correct effective frequency for each source is used when calculating two-point spectral indices.

3.1 Cores

Eight of the eleven sources in the combined sample show 90-GHz core components. In Table 5 we tabulate flux densities for the cores of our sample at centimetre and millimetre wavelengths.

These results show that it is normal for the arcsecond-scale cores of both radio galaxies and quasars to have fairly flat spectra ($\alpha_{\rm cm}^{\rm mm} < 0.5$) over this range of radio frequencies. In most cases the mm-wave flux density is less than the highest value measured at lower wavelengths, which suggests that core spectra typically peak at intermediate frequencies of tens of GHz. However, there is no sign of a cutoff in the spectra of cores by 90 GHz. Similar results have been obtained for other individual low-redshift radio galaxies; for example, Das et al. (2005) detect a 90-GHz core at a level of ~ 15 mJy in the nearby ($z = 0.011$) FRI radio galaxy NGC 3801, which has a 5-GHz core flux density of 3.5 mJy (Croston et al. 2007) while at 8.4 GHz archival VLA observations give a core flux density of 5.9 mJy, implying a substantially inverted spectrum. Studies of core-dominated objects such as blazars at high frequencies (e.g. Bloom et al. 1994) show that flat radio-mm spectra are also typical in those objects. One might expect that our results in this paper would imply that high-redshift radio galaxies would show flat core radio spectra at lower observing frequencies; interestingly, though, this is not consistent with the results of Athreya et al. (1997), who found predominantly steep ($\alpha > 0.5$) spectra at rest-frame frequencies as low as 20–30 GHz in a sample of $z > 2$ radio galaxies. This may be evidence for a true redshift and/or luminosity dependence of the rest-frame behaviour of radio cores, but we emphasise that our sample (by virtue of its selection) is by far from being representative of radio galaxies and lobe-dominated quasars as a whole; observations of a complete sample are required to draw definitive conclusions.

None of the sources for which we have multi-epoch BIMA data shows evidence for strong mm-wave core variability on timescales of months; the core flux densities in individual observations are consistent within the errors. Two of our sources, 3C 123 (Looney & Hardcastle 2000) and Cygnus A (Wright & Sault 1995) show some evidence for variability on longer timescales when the BIMA core flux density is compared with that measured with other instruments. None of our targets is known to have a strongly variable core at longer wavelengths.

3.2 Jets

Jet-related emission is clearly detected in three of the newly observed sources, 3C 388, 3C 401, and 3C 438. This is the first time that FRII jets have been detected at these high radio frequencies. No jet-related emission is detected from five other sources (3C 20, 3C 220.1, 3C 263, 3C 351 and 3C 405) that have known centimetre-wave jet detections, but the jets in these objects are considerably fainter at lower frequencies. The three detected sources are all part of the class of low-excitation radio galaxies with prominent jets and

Table 6. Jet flux densities and two-point spectral indices for sources with detected jets

Jet	Jet flux density (mJy)			Spectral index	
	1.4 GHz	8.4 GHz	BIMA	$\alpha_{1.4}^{8.4}$	$\alpha_{8.4}^{88}$
3C 388 W	63.8 ± 1.9	25.9 ± 0.8	5.7 ± 1.0	0.50 ± 0.02	0.65 ± 0.07
3C 401 S	333 ± 10	129 ± 4	25.5 ± 2.8	0.53 ± 0.02	0.69 ± 0.05
3C 438 N	111 ± 3	44 ± 1	6.2 ± 0.9	0.52 ± 0.02	0.83 ± 0.06
3C 438 S	99 ± 3	30 ± 1	3.3 ± 0.6	0.62 ± 0.02	0.98 ± 0.07

Table 5. Arcsecond-scale core flux densities for the samples at centimetre and millimetre wavelengths

Source	Core flux density (mJy)				
	1.4 GHz	5 GHz	8.4 GHz	15 GHz	BIMA
3C 20		2.6^a	3.3^b		$< 3^c$
3C 123	64^d	93^d	90^d	96^d	42^d
3C 220.1		25^e	27^n		15^g
3C 295			4.6^l		$< 5^g$
3C 388	50^h	62^e	56^m		33^g
3C 401	17^f	32^e	28^f		17^g
3C 405		776^i			887^g
3C 438	7^f		16^f		6^g
3C 263	126^j	157^k	121^j	141^j	108^g
3C 330	$< 5^j$	0.74^a	0.63^l	$< 6^j$	$< 5^g$
3C 351	$< 36^j$	6.5^k	6.5^j		2^g

For simplicity, we do not tabulate the exact frequency of each measurement. Upper limits are 3σ limits based on the off-source noise, except where otherwise stated below. References are as follows: (a) Fernini, Burns & Perley (1997) (b) Hardcastle et al. (1998) (c) Hardcastle & Looney (2001) (d) Looney & Hardcastle (2000) (e) Giovannini et al. (1988) (f) Measured from maps used by Treichel et al. (2001) (g) This paper (h) Measured from map obtained from the 3CRR Atlas (http://www.jb.man.ac.uk/atlas/) (i) Measured from the map of Perley, Dreher & Cowan (1984) (j) Measured from a map used by Hardcastle et al. (2002) (k) Bridle et al. (1994) (l) From maps of Gilbert et al. (2004) (m) Measured from the map used by Kraft et al. (2006) (n) Mullin et al. (2006). For 3C 351, only the southern component of the two described by Bridle et al. (1994) is included in the 5- and 8-GHz flux density measurements, while the 1.4-GHz measurement is considered an upper limit because the resolution is too low to separate the two. Note that this table takes no account of possible core variability at any frequency.

diffuse hotspots, possibly lying in rich environments, identified by Hardcastle et al. (1997).

To investigate the spectra of the jets we used the 1.4 and 8.4-GHz radio maps listed in Table 5 and the full-resolution BIMA datasets. We defined regions on the BIMA maps that include all the apparently jet-related flux density, and then extracted all the apparently jet-related flux density from the (typically much higher resolution) VLA/MERLIN maps. For the GHz-frequency maps the dominant source of (non-systematic) error is the absolute flux density calibration of the images, which we estimate conservatively at 3 per cent. Systematic errors are dominated by the requirement to subtract a background due to the lobes – we did this using identical offset regions adjacent to the jet. For the BIMA images, the thermal noise in the extraction region and the overall estimated flux density calibration error are added in quadrature to give a flux density error estimate. Results are tabulated in Table 6.

In all three of the jet sources we see that the two-point spectral indices between low and high frequencies are significantly inconsistent, in the sense that the spectrum is steeper between cm and mm wavelengths. Thus the spectrum cannot be modelled with a single power law between 1.4 and 90 GHz – a spectral break is required. As the jets in these regions are knotty and complex, a single simple spectral model is probably not appropriate anyway, but it does suggest that these jets are not similar in this respect to FRI jets, which in spite of knotty and complex structure can have a fairly flat spectrum out to the optical and beyond. Chiaberge et al. (2005) report a detection of the 3C 401 jet in *Hubble Space Telescope* near-infrared images, implying a flux density of 6.0 μJy at 190 THz, which would correspond to a spectral index between the mm and infrared of ~ 0.74: thus it seems that the spectrum of the jet breaks at frequencies between 10 and 100 GHz and then remains roughly constant over many decades in frequency. Nothing is known about the high-frequency behaviour of the other two jets, although they are not detected in *Chandra* images.

The brightest non-detected jet in the sample is that of 3C 263 (Bridle et al. 1994), with a radio flux density around 13 mJy: the 3σ upper limit on the 90-GHz flux density from the jet region is 6 mJy, so no interesting limit can be placed on the jet spectral index.

3.3 Hotspots

Almost all of our targets have clear detections of the region at or around the hotspots at 90 GHz. Only the faintest cm-wave hotspots (3C 263 W and 3C 351 S) are undetected in these observations. Since our observations sample a wide range of hotspot structures, we can conclude that it is plausible that few or no FRII hotspots – at least in large, powerful FRIIs – have spectra that cut off below the mm band. This is of course unsurprising in view of the detections of optical, infrared and sometimes X-ray synchrotron radiation from hotspots (Meisenheimer, Yates & Röser 1997; Hardcastle et al. 2004) and the fact that the mm-wave observations probe electron energies only a factor 3 above the highest-frequency cm-wave observations. The high-energy cutoff for particle acceleration is set by the balance between acceleration and loss, and it seems that the very high energy loss rates (implying high photon and/or magnetic field energy densities) required to push that cutoff down to a level where it appears at cm or mm wavelengths are not found in the type of objects we have studied here, though they may be present in some compact steep-spectrum sources (e.g. 3C 196, Hardcastle 2001).

The spectra of the hotspots of many of our sources have been discussed in detail elsewhere [3C 405, Wright et al. (1997); 3C 123, Looney & Hardcastle (2000); 3C 20, Hardcastle & Looney (2001); 3C 263, 3C 330 and 3C 351, Hardcastle et al. (2002)]. In general these results have confirmed what has been known for some time from other work (e.g. Meisenheimer et al. 1989): some sources' hotspots have spectra that are flat up to optical or even X-ray frequencies, while others exhibit a clear spectral steepening either between cm and mm wavelengths, as was the case for 3C 123, or between the mm-wave and the near-infrared. In Table 7 we provide a compilation of radio and mm-wave flux densities for our sample.

Since in general the cm-wavelength maps have higher resolution than the mm-wavelength ones, we adopt the approach (discussed in our earlier papers) of quoting only the flux density of the most compact components accessible to us at radio wavelengths, determined by direct integration with background subtraction where these are well resolved and fitting a Gaussian and baseline when they are not. At 90 GHz we quote flux densities measured by direct integration of the apparently hotspot-related region of the map. This is the correct thing to do if we believe that all the flux density at 90 GHz is due to the hotspot; if there is in fact excess (lobe-related) 90-GHz emission in our integration region, we will tend to overestimate the 90-GHz hotspot flux density, but this seems inevitable without higher-resolution mm-wave observations. We have chosen not to tabulate hotspot flux densities for the three sources (3C 388, 3C 401 and 3C 438) with diffuse hotspots at cm wavelengths, since for these sources we cannot distinguish adequately between hotspots and lobe emission (see section 3.4, below).

The contents of Table 7 are plotted in Fig. 12. This illustrates the wide range of cm-mm spectral indices found in the data (α from ~ 0.6 to ~ 1.5). One trend that is apparent is that in several cases, *within a given source*, brighter hotspots have steeper cm-to-mm spectra ($\alpha_{\rm cm}^{\rm mm}$). In several of these objects the brighter hotspots are large secondaries (as in 3C 20, 3C 351 and 3C 405) and so this may be connected to the observation that large diffuse secondary hotspots in multiple-hotspot sources tend not to show X-ray synchrotron radiation (Hardcastle, Croston & Kraft 2007); as discussed in previous work (e.g. Hardcastle & Looney 2001) there is little evidence for spectral ageing effects in secondary hotspots at these frequencies. The data also hint that more luminous hotspots have steeper $\alpha_{\rm cm}^{\rm mm}$, but there are insufficient sources to carry out meaningful statistical comparisons.

3.4 Lobes

It is very clear that hotspots, cores and (where present) jets dominate the high-frequency radio emission from these sources. Nevertheless some sources show clear emission from lobe regions. These are 3C 20 and 3C 123 (as described in our earlier papers), 3C 405 (where a spur of emission leading N and W from the E hotspot is seen) and 3C 388 (where the W hotspot is extended to the SE). In all four of these cases the 'lobe' emission at mm wavelengths is well matched morphologically to high-surface-brightness features close to the hotspot at cm wavelengths. As noted above, extended emission in 3C 388 E, 3C 401 and 3C 438 cannot unambiguously be associated with either the lobes or the hotspots, but it is plausible that some or all of this emission is also related to the lobes. No lobe-related emission is seen in 3C 220.1 or 3C 295, though of course these are the highest-redshift sources in our sample with observing frequencies corresponding to $\gtrsim 140$ GHz in the source frame.

In Fig. 13 we show maps of spectral index between 8.4 and 90 GHz for the four small sources with detected emission that might be lobe-related. 3C 20 (as already discussed in Hardcastle & Looney 2001) and 3C 388 show clear spectral steepening away from the hotspots. In 3C 401 and 3C 438 the flattest-spectrum regions are the jets (already discussed above) and there is no clear evidence for resolved spectral steepening in the lobes.

We concentrate initially on the sources with clear detections of lobe-related emission at 90 GHz: 3C 20, 3C 123, 3C 388 and 3C 405. The spectra of the lobes of the first two is discussed in our earlier papers: we measured flux densities in matched regions defined using the 90-GHz maps for 3C 388 and 3C 405. In all of these sources we find that the spectral index between cm wavelengths (5 or 8 GHz) and 90 GHz is steeper in the extended emission than in the corresponding hotspot, which is qualitatively consistent with expectations from spectral ageing models. However, if there is any curvature in the hotspot spectra (as there is in the spectra of the 3C 123 and 3C 405 hotspots) then a simple decrease in the magnetic field strength and electron energy, as expected if plasma expands adiabatically on leaving the hotspots, would also produce such a result. As discussed in Section 1, we showed in the case of the peculiar object 3C 123 that the spectrum of the detected northern lobe region is inconsistent with a Jaffe & Perola (1973; hereafter J-P) spectral ageing model, perhaps a result of particle reacceleration in the lobe. By contrast the spectrum of the 3C 20 E lobe is well fitted with a J-P model provided that the 'injection index' (the low-frequency spectral index) is tuned to allow a good fit to the low-frequency data. In 3C 388, the only other source where we have multi-frequency data on the lobes readily available, we find that the same is true – a J-P model provides a good fit to the data from the W lobe provided that the injection index is ~ 0.7. Our data are not sensitive enough to take the next step and produce maps of spectral age as a function of position to test whether the spectral ages required are physically reasonable and/or consistent with what is found at lower frequencies.

For the sources with undetected lobes (3C 220.1 and 3C 295) we can only set lower limits on the spectral indices of any undetected lobe emission of $\alpha_{8.4}^{90}$ (lab frame) > 1.2 for both sources. This is consistent with the measured spectral indices in the steepest-spectrum regions of other sources (Fig. 13) and so there is little evidence for a difference in physical behaviour in these two objects.

4 DISCUSSION

4.1 Summary: radio galaxies at 90 GHz

Our observations have now detected at 90 GHz the synchrotron emission from arcsec-scale components of FRII radio galaxies seen at lower frequencies: cores, jets, hotspots and lobes. We can summarize our results and their consequences as follows:

- Cores are flat-spectrum up to 90 GHz in most cases, implying that synchrotron self-absorption continues to be important in the cores well above cm wavelengths.
- Bright jets are detected and show curved or broken power-law spectra, which is interesting given that the mechanism of particle acceleration in FRII jets is not well known at present. Particle acceleration in jets is required for the jets to be visible (unless they are simply boundary-layer effects) but is essentially ignored in most models of particle acceleration and energy transport in FRIIs. The jets we see at 90 GHz are predominantly in objects with atypically bright cm-wavelength jets, though, and it is not clear that they tell us what will be seen when more typical FRII sources are observed with higher sensitivity.
- Hotspots have been known for some time to be bright sources at 90 GHz and beyond, and are clearly detected in all of our targets that show compact, bright hotspots at lower frequencies. This is unsurprising given the known detections of hotspots (including several in our sample) at infrared, optical and X-ray wavelengths in synchrotron emission. The wide variety of spectral indices seen between 8 and 90 GHz indicates that hotspots have significantly different electron energy spectra by energies corresponding to 90-GHz synchrotron emission.
- Emission from the lobes is not universal but is common in our

Table 7. Hotspot flux densities for the samples at centimetre and millimetre wavelengths

Source	Hotspot	Flux density (Jy)				
		1.4 GHz	5 GHz	8.4 GHz	15 GHz	BIMA
3C 20	W	2.661	1.112	0.714	0.413	0.118
	NE		0.137	0.087	0.061	0.021
	SE	1.257	0.486	0.289	0.171	0.037
3C 123	E		6.372	4.277	2.392	0.288
	W	0.867	0.345	0.222	0.112	0.018
3C 220.1	E			0.059		0.010
	W			0.032		0.008
3C 295	N	2.545	1.089	0.643	0.356	0.080
	S	0.231	0.102	0.582	0.352	0.111
3C 405	A	93	38		13.8	1.38
	B		10.7			0.61
	D	104	50		21	1.48
3C 263	E	1.670	0.591	0.303	0.184	0.054
	W		0.023	0.016	0.009	< 0.004
3C 330	E	3.830		0.755	0.376	0.025
	W			0.079†		0.018
3C 351	N (J)	0.530		0.130	0.088	0.017
	N(L)	1.30		0.316	0.201	0.028
	S	< 0.017		0.003	0.0017	< 0.003

Upper limits are 3σ limits based on the off-source noise. References are as follows: 3C 20, Hardcastle & Looney (2001) (we tabulate the 'compact' component values for the NE hotspot but the 'region' values for the W hotspot); 3C 123, Looney & Hardcastle (2000); 3C 263, 3C 330 & 3C 351, Hardcastle et al. (2002); 3C 295, radio flux densities from Harris et al. (2000); 3C 405 hotspots A and D, radio flux densities from Carilli et al. (1991); all other values, this paper. For 3C 405 we use the conventional notation of Carilli et al. (1991) to label the hotspots; hotspot A and B are respectively the secondary and primary hotspots in the W lobe and D the brightest hotspot in the E lobe. Similarly for 3C 351 we use the notation of Bridle et al. (1994), in which J is the compact primary hotspot and L is the secondary.

† We take the opportunity to correct the incorrectly transcribed flux density for 3C 330 W that was quoted by Hardcastle et al. (2002).

sample of high-surface-brightness targets; it comes preferentially from high-surface-brightness regions of lower-frequency emission close to the hotspots. Spectral indices in the lobes between cm and mm wavelengths are typically steep, $\alpha > 1.0$, and so qualitatively the properties of the lobes are consistent with the standard spectral ageing model. In a few cases we have been able to show quantitative consistency with a Jaffe & Perola (1973: J-P) electron spectrum, though in at least one case (3C 123) we have argued elsewhere that reacceleration in the lobes may be required to produce the high-frequency emission.

4.2 Prospects for ALMA and the EVLA

The observations summarized in this paper give a preview of the components that ALMA may be expected to detect when it observes FRII radio galaxies at frequencies around 90 GHz. However, ALMA will have instantaneous sensitivity an order of magnitude higher than BIMA, substantially better uv plane coverage, and higher angular resolution. The increase in our capability to image mm-wave structures in extragalactic radio sources will be comparable to that obtained at cm wavelengths when the VLA first became available at the end of the 1970s. Our work here has shown that there are questions that only ALMA can answer regarding the detailed spectral structure of radio galaxies. Since the synchrotron spectra of lobes, particularly near the hotspots, appear to be cutting off in the mm regime, ALMA will provide the best possible leverage on models of spectral ageing and therefore of energy transport and particle dynamics in the lobes. ALMA should also be able to probe the high-frequency structure of FRII jets for the first time. We emphasise however that these projects will require us to combine mm observations with observations at lower frequencies with instruments like the (expanded) VLA, bearing in mind that the VLA will have greatly increased sensitivity at frequencies of tens of GHz once the EVLA upgrade is complete. Higher ALMA frequencies will be of value in studies of hotspots but will probably not probe deep into the lobes, and the increasingly small ALMA field of view at high frequencies will probably prove restrictive in this respect. The requirement for complementary observations at lower radio frequencies is a motivation for studies of equatorial samples of lobe-dominated radio galaxies in the run-up to the ALMA era (e.g. Best, Röttgering & Lehnert 1999).

One intriguing possible use of ALMA is in the direct detection of the expected Sunzaev-Zel'dovich (S-Z) effect from radio galaxy lobes (Enßlin & Kaiser 2000; Colafrancesco 2008). Since X-ray inverse-Compton emission from the lobes of radio galaxies is now routinely detected (e.g. Kataoka & Stawarz 2005; Croston et al. 2005) we know the electron content of radio lobes well enough to make predictions at the level of individual radio galaxies, and signatures of the S-Z effect may well in principle be detectable at mm wavelengths, with the possibility of providing information about the low-energy electron spectrum (Colafrancesco 2008). Apart from the weakness of the signal, the major difficulty is the synchrotron emission at these wavelengths. Our work in this paper shows that emission from cores and hotspots is likely to be unavoidable, at least in active radio galaxies as opposed to relics. However, some hope is provided by the (limited) evidence that spectral ageing may be operating as expected at high frequencies in these lobes. In the (most favourable) case of effective pitch angle scattering (i.e., a J-P spectrum), assuming losses dominated by a

constant, fully tangled magnetic field of strength B, the maximum Lorentz factor in the electron spectrum is

$$\gamma_{\rm c} = \frac{3m_{\rm e}c}{4\sigma_{\rm T}}\frac{1}{Ut} \quad (1)$$

(Pacholczyk 1970) where $\sigma_{\rm T}$ is the Thomson cross-section, $m_{\rm e}$ is the mass of the electron, U is the energy density in the magnetic field ($U = B^2/2\mu_0$) and t is the ageing time. This energy corresponds to a characteristic 'break' frequency given by

$$\nu_{\rm b} = \frac{3}{4\pi}\gamma_{\rm c}^2\frac{eB}{m_{\rm e}} \quad (2)$$

(Longair 1994) where e is the charge on the electron, and so

$$\nu_{\rm b} = \frac{243\pi}{4}\frac{m_{\rm e}^5c^2}{e^7\mu_0^2B^3t^2} \quad (3)$$

(Leahy 1991). As shown graphically by Jaffe & Perola (1973) and Leahy (1991), the synchrotron spectrum rapidly steepens at frequencies at and around $\nu_{\rm b}$. Because the steepening in the J-P spectrum is monotonic, there is a unique value of the break frequency that produces a flux density ratio R between two observed frequencies ν_1, ν_2 (s.t. $\nu_2/\nu_1 = f$) if the spectrum is a power law at frequencies $\ll \nu_{\rm b}$ with a spectral index (the 'injection index') α and $-\log(R)/\log(f) > \alpha$. Fig. 14 shows a plot of the log of R as a function of $\nu_1/\nu_{\rm b}$ for various values of f and a plausible choice of α. Required values of the break frequency can be read from this plot. For example, if we know that the flux density at $\nu_1 = 8.4$ GHz (source frame) is 1 Jy, which is at the high end of what is observed for a typical 3CRR source, and we require the flux density at $\nu_2 = 90$ GHz to be < 1 μJy (i.e., well below any detectable S-Z effect), $\log_{10}(f) \approx 1$, $\log_{10}(R) = -6$ and Fig. 14 shows that $\nu_{\rm b} \approx \nu_1$. We can then use eq. 3 to find the required age of the plasma for a given magnetic field strength. For typical observed magnetic fields ~ 1 nT (Croston et al. 2005) we require lobe ages (i.e. times since particle acceleration) of $\gtrsim 2 \times 10^7$ years, which will be achieved only in large, old radio galaxies; ages comparable to this are however found in some spectral ageing studies (e.g. Alexander & Leahy 1987). Because $t \propto 1/\sqrt{\nu}_b$, Fig. 14 shows that these conclusions only change weakly if we are searching for the S-Z effect at higher frequencies. However, there is a strong dependence on the magnetic field strength, so more powerful radio galaxies with higher magnetic field strengths may be better targets. Large radio galaxies are in general the best targets for S-Z detections, both because spectral ageing will have had the greatest effect and because the integrated S-Z decrement (for a given low-energy electron spectrum) is essentially proportional to the energy stored in the lobes, but in practice there will be a tradeoff between these factors and the requirement that the source be well imaged in ALMA's small field of view. Nevertheless we consider that S-Z detection experiments, while challenging, are not completely ruled out by what our observations have shown us about the nature of radio galaxies at ALMA frequencies.

We emphasise that the calculation we have carried out here assumes that the J-P electron spectrum is a completely accurate description of the lobes. If there is even a very small amount of local particle reacceleration in radio galaxy lobes, or (equivalently) rapid transport of high-energy electrons from the hotspots, then the flat-spectrum radiation produced will completely dominate the mm-wave emission from the lobes in 'old' regions of plasma far from the hotspots (potentially in the manner we saw in our observations of 3C 123; Looney & Hardcastle 2000). Another way of interpreting the calculations above is that they show ALMA's ability to provide a very sensitive probe of the degree to which local particle acceleration is important in lobes. Thus deep ALMA observations of old radio lobes are likely to produce interesting results whether they detect the S-Z effect or not.

ACKNOWLEDGEMENTS

We thank Mel Wright for providing us with the calibrated Cygnus A data and images, and the referee, Prof. D.J. Saikia, for constructive comments that have helped us improve the paper. MJH thanks the Royal Society for a research fellowship. LWL acknowledges support from the Laboratory for Astronomical Imaging at the University of Illinois and NSF grant AST 0228953. The National Radio Astronomy Observatory is a facility of the National Science Foundation operated under cooperative agreement by Associated Universities, Inc.

REFERENCES

Alexander, P., Leahy, J.P., 1987, MNRAS, 224, 1
Athreya, R.M., Kapahi, V.K., McCarthy, P.J., van Breugel W., 1997, ApJ, 289, 525
Baars, J.W.M., Genzel, R., Pauliny-Toth, I.I.K., Witzel, A., 1977, A&A, 61, 99
Best, P.N., Röttgering, H.J.A., Lehnert, M.D., 1999, MNRAS, 310, 223
Bloom, S.D., Marscher, A.P., Gear, W.K., Terasranta, H., Valtaoja, E., Aller, H.D., Aller, M.F., 1994, AJ, 108, 398
Bridle, A.H., Hough, D.H., Lonsdale, C.J., Burns, J.O., Laing, R.A., 1994, AJ, 108, 766
Carilli, C.L., Perley, R.A., Dreher, J.W., Leahy, J.P., 1991, ApJ, 383, 554
Chiaberge, M., et al., 2005, ApJ, 629, 100
Colafrancesco, S., 2008, MNRAS in press (arXiv:0801.4535)
Croston, J.H., Hardcastle, M.J., Harris, D.E., Belsole, E., Birkinshaw, M., Worrall, D.M., 2005, ApJ, 626, 733
Croston, J.H., Kraft, R.P., Hardcastle, M.J., 2007, ApJ, 660, 191
Das, M., Vogel, S.N., Verdoes Kleijn, G.A., O'Dea, C.P., Baum, S.A., 2005, ApJ, 629, 757
Dreher, J.W., Perley, R.A., Cowan, J.J., 1984, ApJ, 285, L35
Edelson, R.A., 1987, AJ, 94, 1150
Enßlin, T.A., Kaiser, C.R., 2000, A&A, 360, 417
Fanaroff, B.L., Riley, J.M., 1974, MNRAS, 167, 31P
Fernini, I., Burns, J.O., Perley, R.A., 1997, AJ, 114, 2292
Gilbert, G., Riley, J.M., Hardcastle, M.J., Croston, J.H., Pooley, G.G., Alexander, P., 2004, MNRAS, 351, 845
Giovannini, G., Feretti, L., Gregorini, L., Parma, P., 1988, A&A, 199, 73
Hardcastle, M.J., 2001, A&A, 373, 881
Hardcastle, M.J., Looney, L.W., 2001, MNRAS, 320, 355
Hardcastle, M.J., Alexander, P., Pooley, G.G., Riley, J.M., 1997, MNRAS, 288, 859
Hardcastle, M.J., Alexander, P., Pooley, G.G., Riley, J.M., 1998, MNRAS, 296, 445
Hardcastle, M.J., Birkinshaw, M., Cameron, R., Harris, D.E., Looney, L.W., Worrall, D.M., 2002, ApJ, 581, 948
Hardcastle, M.J., Harris, D.E., Worrall, D.M., Birkinshaw, M., 2004, ApJ, 612, 729
Hardcastle, M.J., Croston, J.H., Kraft, R.P., 2007, ApJ, 669, 893
Harris, D.E., et al., 2000, ApJ, 530, L81
Jaffe, W.J., Perola, G.C., 1973, A&A, 26, 423 [J-P]
Kataoka, J., Stawarz, Ł., 2005, ApJ, 622, 797
Katz-Stone, D.M., Rudnick, L., Anderson, M.C., 1993, ApJ, 407, 549
Kraft, R.P., Azcona, J., Forman, W.R., Hardcastle, M.J., Jones, C., Murray, S.S., 2006, ApJ, 639, 753
Laing, R.A., Riley, J.M., Longair, M.S., 1983, MNRAS, 204, 151
Leahy, J.P., 1991, in Hughes P.A., ed., Beams and Jets in Astrophysics, Cambridge University Press, Cambridge, p. 100

Longair, M.S., 1994, High energy astrophysics, Cambridge University Press, Cambridge
Looney, L.W., Hardcastle, M.J., 2000, ApJ, 534, 172
Meisenheimer, K., Röser, H.-J., Hiltner, P.R., Yates, M.G., Longair, M.S., Chini, R., Perley, R.A., 1989, A&A, 219, 63
Meisenheimer, K., Yates, M.G., Röser, H.-J., 1997, A&A, 325, 57
Myers, S.T., Spangler, S.R., 1985, ApJ, 291, 52
Pacholczyk, A.G., 1970, Radio Astrophysics, Freeman, San Francisco
Perley, R.A., Dreher, J.W., Cowan, J.J., 1984, ApJ, 285, L35
Mullin, L.M., Hardcastle, M.J., Riley, J.M., 2006, MNRAS, 372, 510
Roettiger, K., Burns, J.O., Clarke, D.A., Christiansen, W.A., 1994, ApJ, 421, L23
Rudnick, L., 1999, in J. Biretta et al., eds, Life Cycles of Radio Galaxies, New Astronomy Reviews (astro-ph/9910202)
Salter, C.J., et al., 1989, A&A, 220, 42
Sault, R.J., Teuben, P.J., Wright, M.C.H., 1995, in Shaw R.A., Payne H.E., Hayes J.J.E., eds, Astronomical Data Analysis Software and Systems IV, ASP Conference Series 77, San Francisco, p. 33
Steppe, H., Salter, C.J., Chini, R., Kreysa, E., Brunswig, W., Lobato, Perez, J., 1988, A&AS, 75, 317
Steppe, H., Jeyakumar, S., Saikia, D.J., Salter, C.J., 1995, A&AS, 113, 409
Treichel, K., Rudnick, L., Hardcastle, M.J., Leahy, J.P., 2001, ApJ, 561, 691
Wright, M., Birkinshaw, M., 1984, ApJ, 281, 135
Wright, M.C.H., Sault, R.J., 1993, ApJ, 402, 546
Wright, M.C.H., Chernin, L.M., Forster, J.R., 1997, ApJ, 483, 783

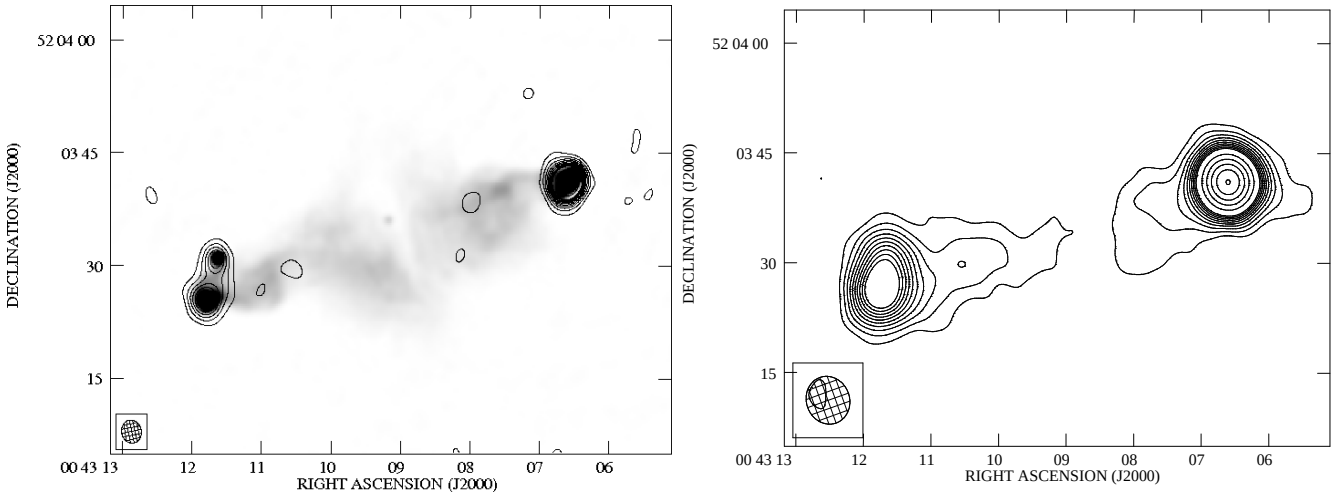


Figure 1. BIMA images of 3C 20. Left: contours of a 3.1×2.6-arcsec resolution map (beam position angle $11.5°$) are superposed on a greyscale 1.1-arcsec 8.4-GHz VLA image (Hardcastle et al. 1997). Right: a 6.6×5.9-arcsec resolution BIMA map (beam position angle $19.7°$). Contours are at $-2, -1, 1, 2, 3, \ldots, 10, 15, \ldots 50, 60, \ldots 100$ times the 3σ level, which is 2.9 mJy beam^{-1} for the high-resolution map and 3.4 mJy beam^{-1} for the low-resolution one.

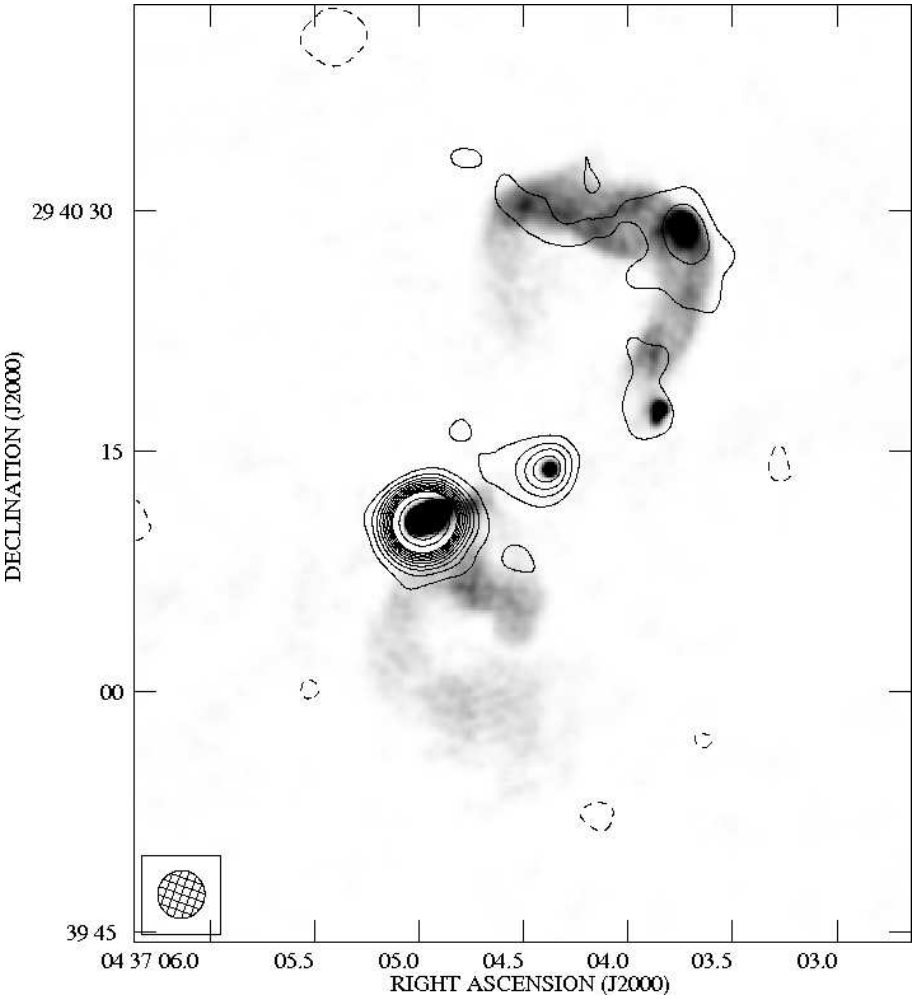


Figure 2. BIMA image of 3C 123. Contours of a 3.0×2.9-arcsec resolution map (beam position angle $-19.6°$) are superposed on a greyscale 0.6-arcsec 8.4-GHz VLA image (Hardcastle et al. 1997). Contours as for Fig. 1: the 3σ level is at 9.0 mJy beam^{-1}.

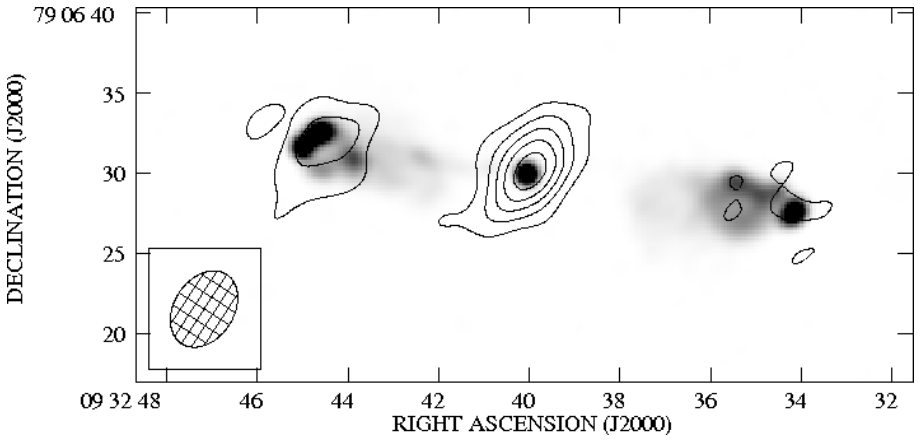


Figure 3. BIMA image of 3C 220.1. Contours of a 5.2×3.7-arcsec resolution map (beam position angle $-33.2°$) are superposed on a greyscale 0.6-arcsec 8.4-GHz VLA image (Mullin et al. 2006). Contours as for Fig. 1: the 3σ level is at 2.6 mJy beam^{-1}.

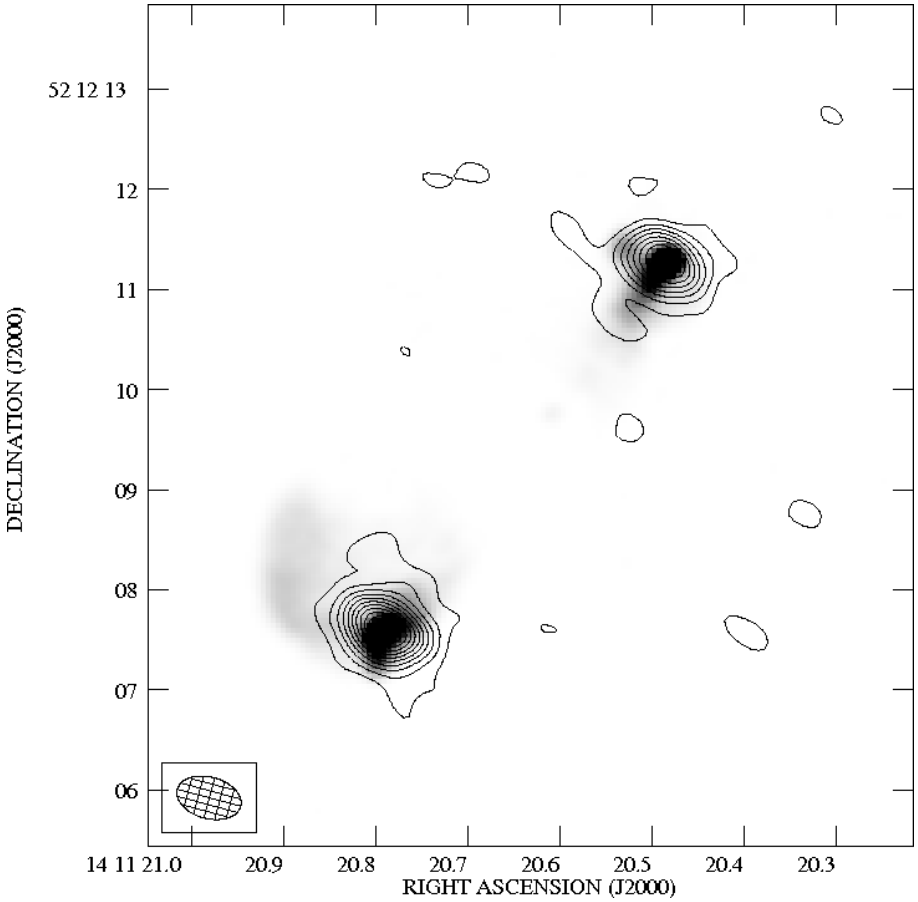


Figure 4. BIMA image of 3C 295. Contours of a 0.65×0.41-arcsec resolution map (beam position angle $74.9°$) are superposed on a greyscale 0.18×0.17-arcsec 8.5-GHz VLA image (beam position angle $13.8°$; Gilbert et al. 2004). Contours as for Fig. 1: the 3σ level is at 5.3 mJy beam^{-1}.

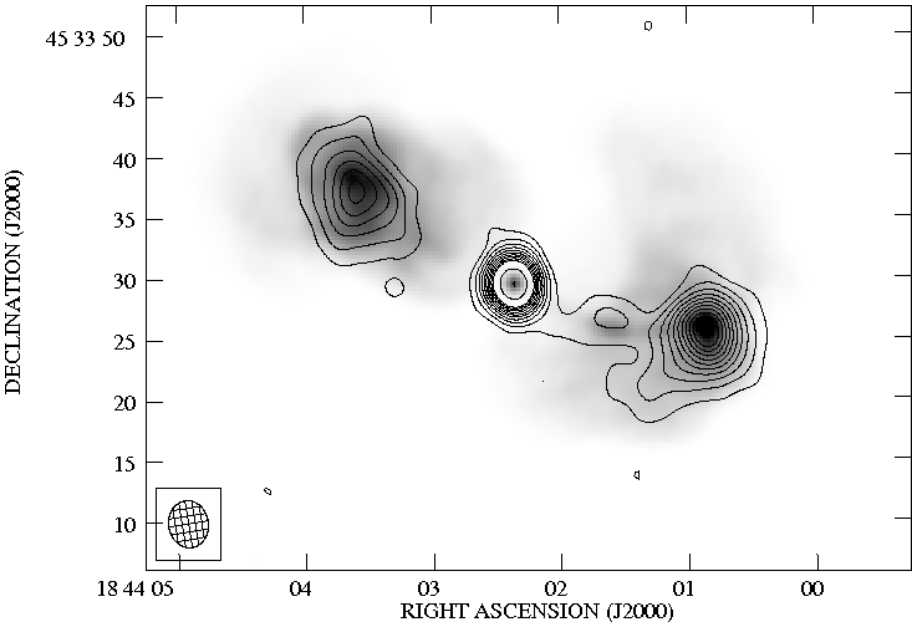


Figure 5. BIMA image of 3C 388. Contours of a 3.88×3.27-arcsec resolution map (beam position angle $8.9°$) are superposed on a greyscale 1.32-arcsec 1.4-GHz VLA image (Roettiger et al. 1994). Contours as for Fig. 1: the 3σ level is at 1.6 mJy beam^{-1}.

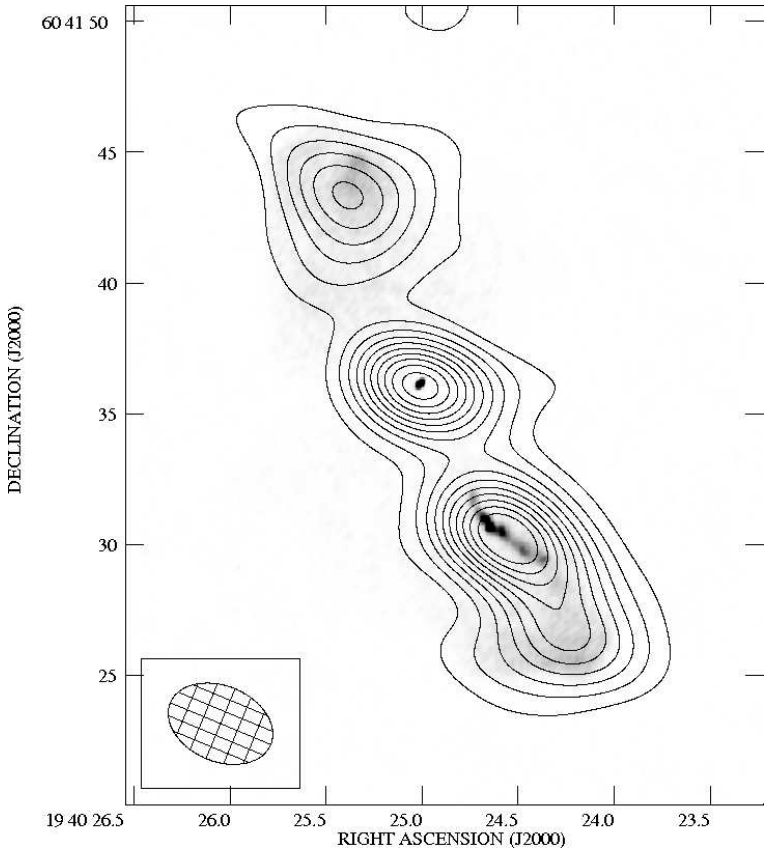


Figure 6. BIMA image of 3C 401. Contours of a 4.16×2.89-arcsec resolution map (beam position angle $67.4°$) are superposed on a greyscale 0.25×0.17-arcsec 8.4-GHz VLA image (beam position angle $-36.0°$; Hardcastle et al. 1997). Contours as for Fig. 1: the 3σ level is at 1.2 mJy beam^{-1}.

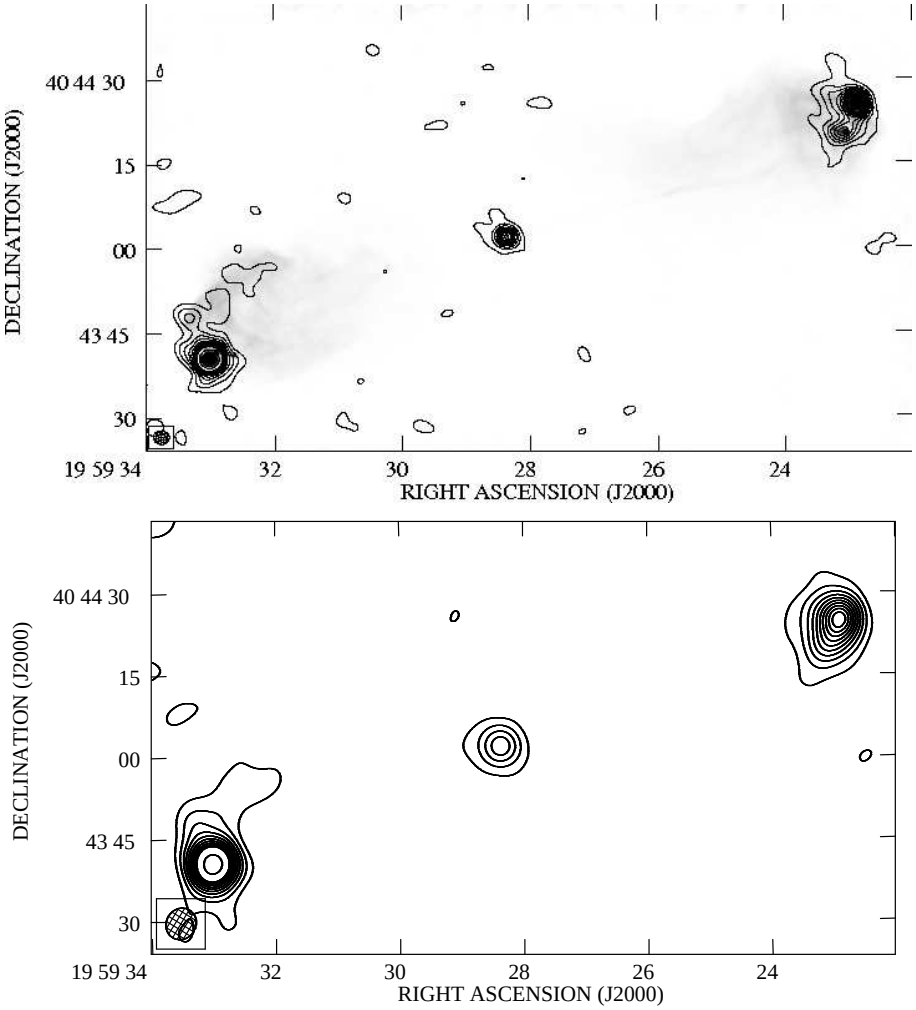


Figure 7. BIMA image of Cygnus A (3C 405). Top: contours of a 2.83×2.44-arcsec resolution map (beam position angle $60.8°$) are superposed on a greyscale 0.4-arcsec 4.9-GHz VLA image (Dreher, Perley & Cowan 1984). Bottom: a 5.93×5.43-arcsec resolution map (beam position angle $-31.7°$). Contours as for Fig. 1: the 3σ level for the first map is 60 mJy beam^{-1} and for the second is 160 mJy beam^{-1}, including in both cases the effects of positive bias from the maximum entropy routine used for the deconvolution.

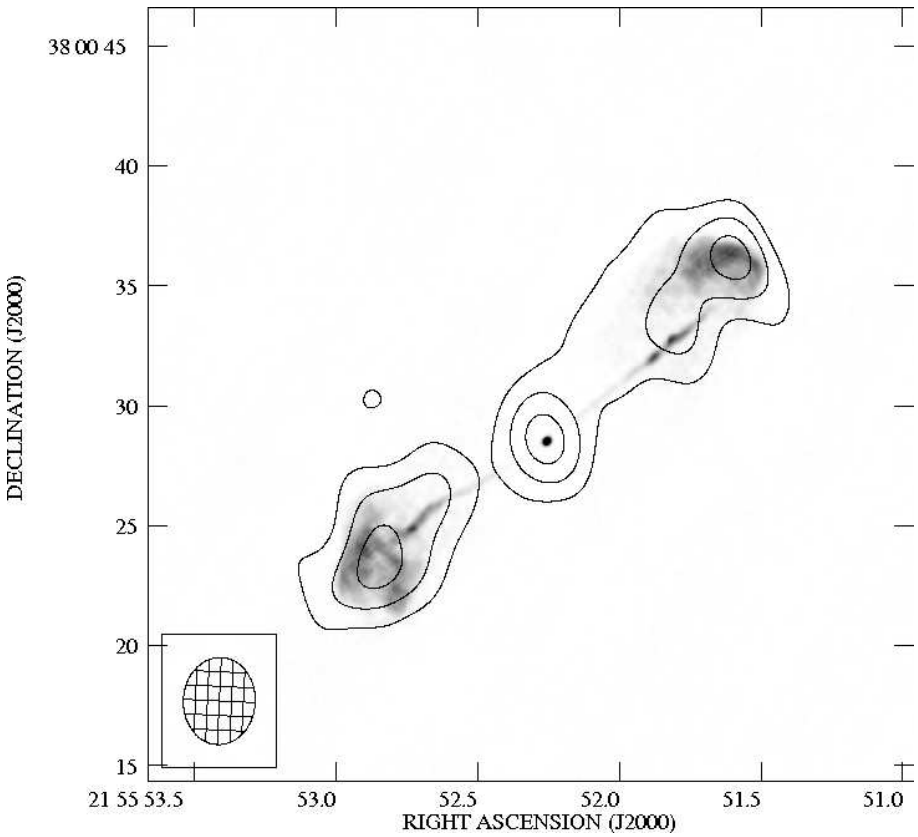


Figure 8. BIMA image of 3C 438. Contours of a 3.63×3.00-arcsec resolution map (beam position angle $-2.7°$) are superposed on a greyscale 0.25×0.21-arcsec 8.4-GHz VLA image (beam position angle $-47.8°$; Hardcastle et al. 1997). Contours as for Fig. 1: the 3σ level is at 1.8 mJy beam^{-1}.

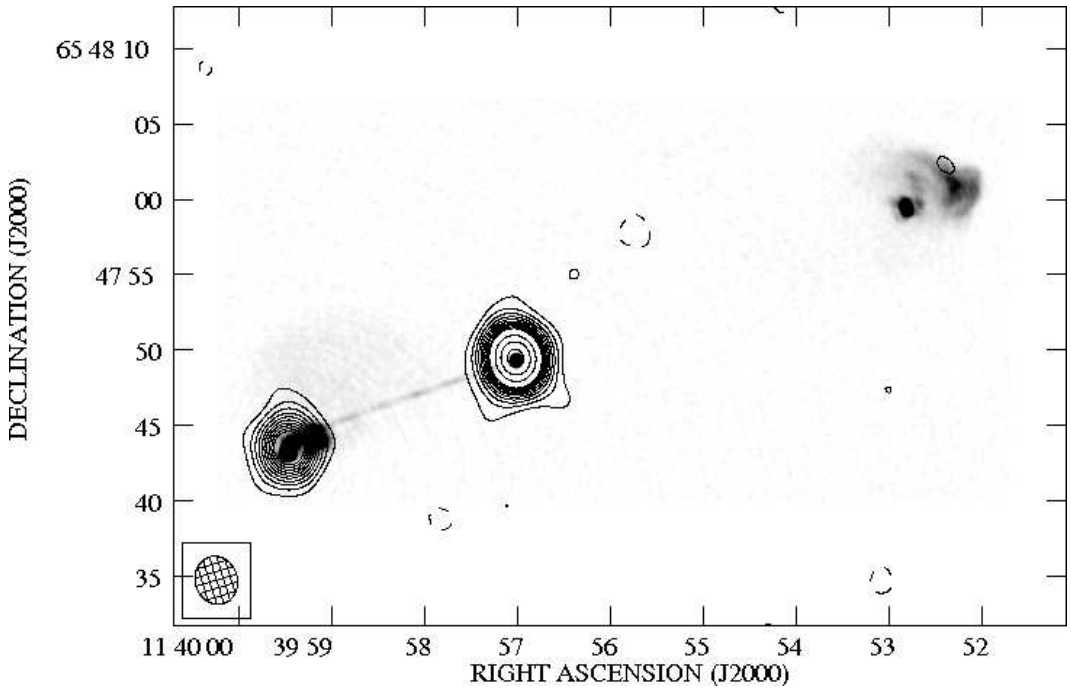


Figure 9. BIMA image of 3C 263. Contours of a 3.22×2.79-arcsec resolution map (beam position angle $17.0°$) made with B-configuration data only are superposed on a greyscale 0.36-arcsec 4.9-GHz VLA image (Bridle et al. 1994). Contours as for Fig. 1: the 3σ level is at 1.1 mJy beam^{-1}.

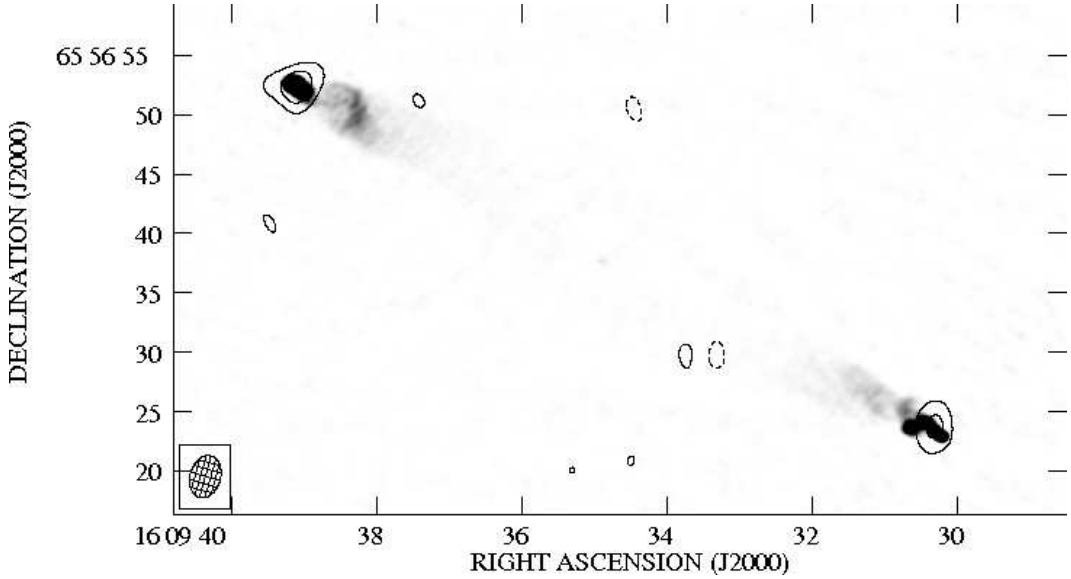


Figure 10. BIMA image of 3C 330. Contours of a 3.61×2.56-arcsec resolution map (beam position angle $29.1°$) made with B-configuration data only are superposed on a greyscale 0.57×0.48-arcsec 8.4-GHz VLA image (beam position angle $76.7°$; Gilbert et al. 2004). Contours as for Fig. 1: the 3σ level is at 2.7 mJy beam^{-1}.

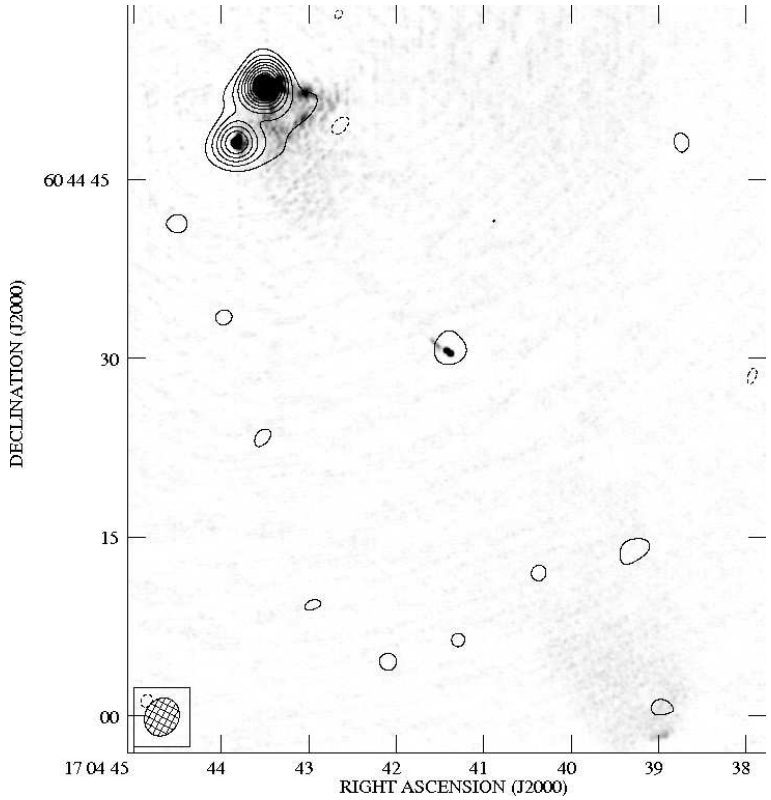


Figure 11. BIMA image of 3C 351. Contours of a 3.28×2.83-arcsec resolution map (beam position angle $-28.0°$) made with B-configuration data only are superposed on a greyscale 0.3-arcsec 8.4-GHz VLA image (Gilbert et al. 2004). Contours as for Fig. 1: the 3σ level is at 0.94 mJy beam^{-1}.

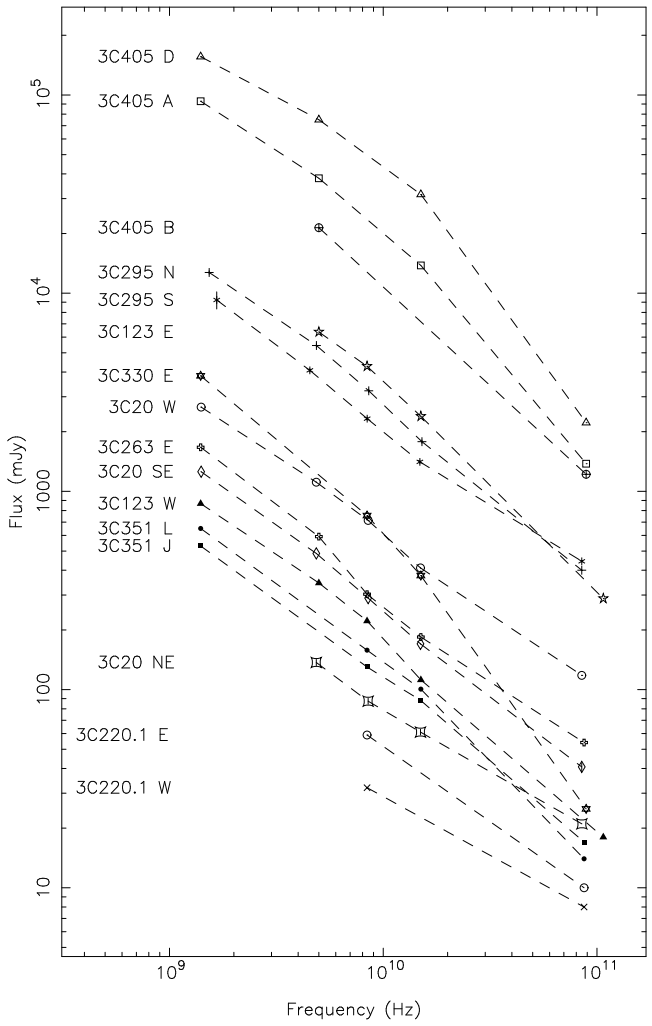


Figure 12. Spectra of the BIMA-detected hotspots listed in Table 7. Some flux densities have been scaled for clarity. 3C 405 D has been increased by a factor 1.5; 3C 405 B, 2.0; 3C 295 N, 5.0; 3C 295 S, 4.0; 3C 351 L, 0.5.

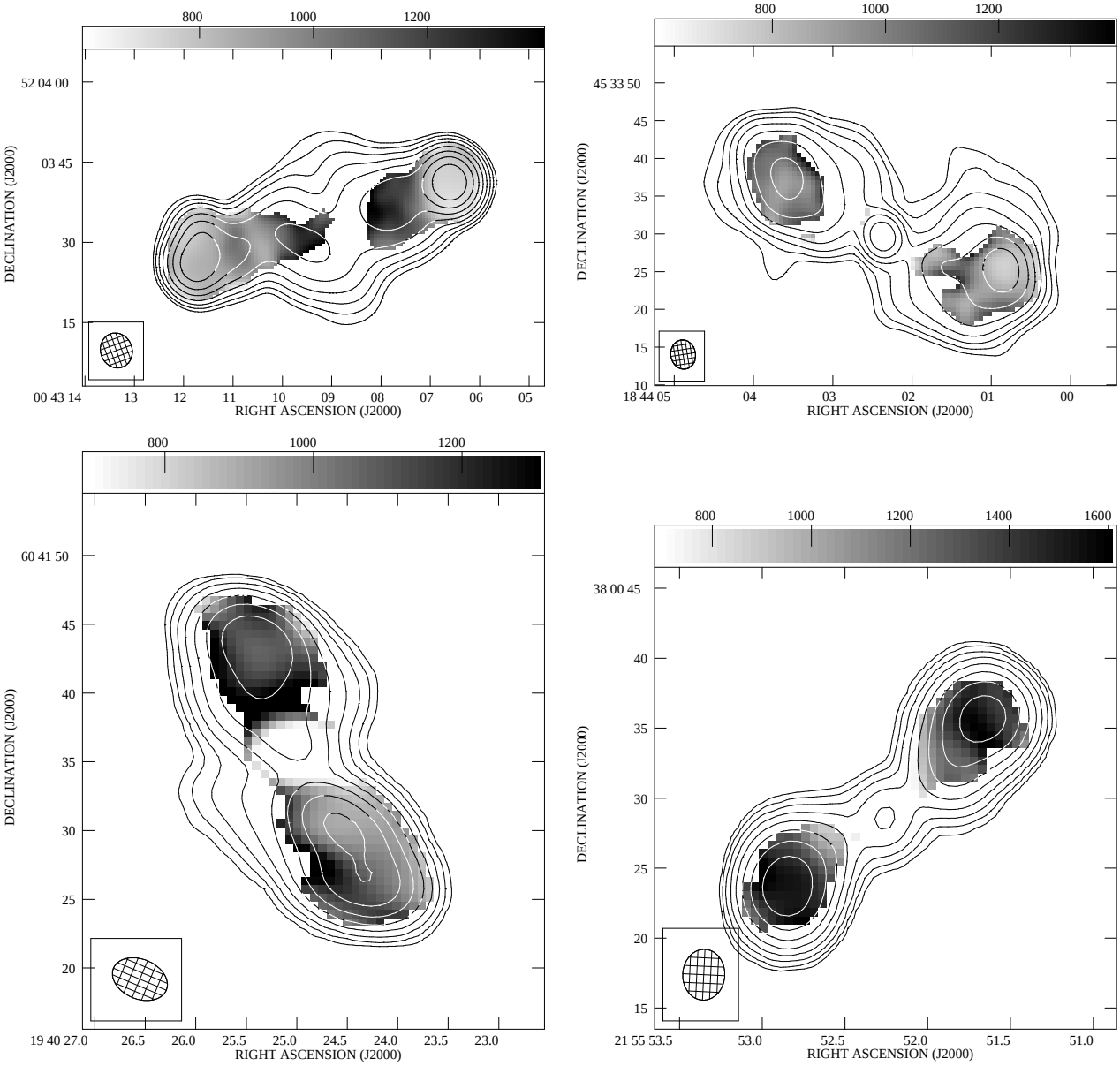


Figure 13. Maps of spectral index between 8.4 GHz and 90 GHz. Top left: 3C 20 at 6.6×5.9 arcsec resolution (beam position angle $19.7°$). Top right: 3C 388 at 3.88×3.27 arcsec (position angle $8.8°$). Bottom left: 3C 401 at 4.19×2.89 arcsec (position angle $67.3°$). Bottom right: 3C 438 at 3.63×3.00 arcsec (position angle $-2.8°$). Colour bars at the top of images are in units of $1000 \times \alpha_{8.4}^{90}$. Contours overlaid are from matched-resolution 8.4-GHz maps in each case. These maps were made from the VLA uv data used by Hardcastle et al. (1997), Kraft et al. (2006), Hardcastle et al. (1997) and Treichel et al. (2001) respectively. White contours are used when the underlying spectral index map is dark.

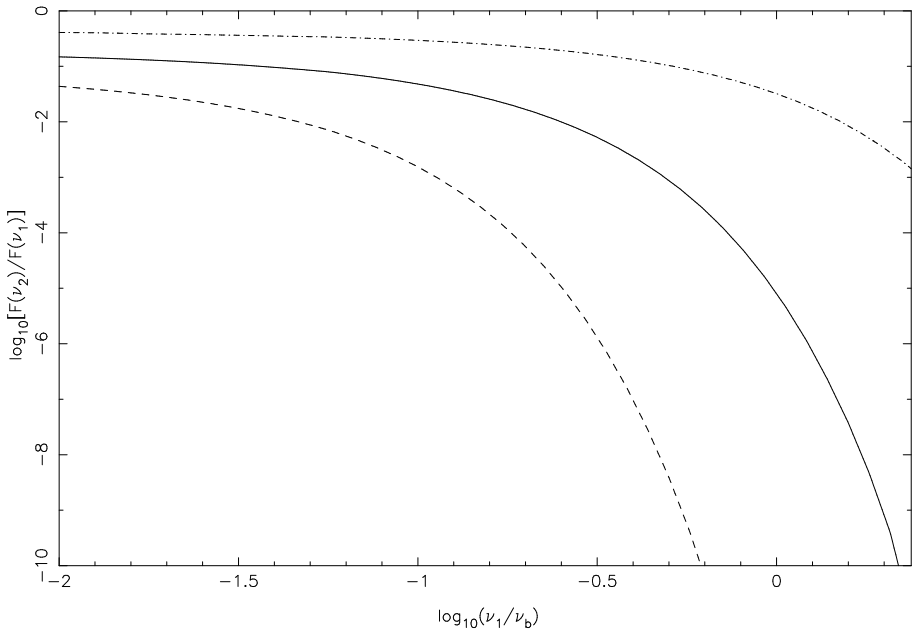


Figure 14. The ratio of flux densities at two source-frame frequencies ν_1 and ν_2 as a function of $\nu_1/\nu_{\rm b}$, where $\nu_{\rm b}$ is the break frequency defined in eq. 3. A Jaffe & Perola (1973) electron energy spectrum is assumed. The dashed line corresponds to $\log_{10}(\nu_2/\nu_1) = 1.5$, the solid line to $\log_{10}(\nu_2/\nu_1) = 1.0$ and the dotted line to $\log_{10}(\nu_2/\nu_1) = 0.5$. The low-frequency spectral index ('injection index') $\alpha = 0.7$ in this plot.